Design and Optimization of Electrically Injected InP-Based Microdisk Lasers Integrated on and Coupled to a SOI Waveguide Circuit

Joris Van Campenhout, *Student Member, IEEE*, Pedro Rojo Romeo, Dries Van Thourhout, *Member, IEEE*, Christian Seassal, Philippe Regreny, Lea Di Cioccio, Jean-Marc Fedeli, and Roel Baets, *Fellow, IEEE*

***Abstract*—We have performed a numerical study involving the design and optimization of InP-based microdisk lasers integrated on and coupled to a nanophotonic silicon-on-insulator (SOI) waveguide circuit, fabricated through bonding technology. The theoretical model was tested by fitting it to the lasing characteristics obtained for fabricated devices, which we presented previously. A good fit was obtained using parameter values that are consistent with numerical simulation. To obtain optimized laser performance, the composition of the InP-based epitaxial layer structure was optimized to minimize internal optical loss for a structure compatible with efficient current injection. Specific attention was paid to a tunnel-junction based approach. Bending loss was quantified to estimate the minimum microdisk diameter. The coupling between the InP microdisk and Si waveguide was calculated as function of the bonding layer thickness, waveguide offset and waveguide width. To study the lateral injection efficiency, an equivalent electrical network was solved and the voltage-current characteristic was calculated. Based on these results, the dominant device parameters were identified, including microdisk thickness and radius, coupling loss and tunnel-junction p-type doping. These parameters were optimized to obtain maximum wall-plug efficiency, for output powers in the range 1–100 μW. The results of this optimization illustrate the potential for substantial improvement in laser performance.**

***Index Terms*—Heterogeneous integration, InGaAsP, integrated optics, microdisk laser, optical interconnect, Si.**

I. Introduction

OVER the last twenty years, microdisk lasers have shown good potential as compact and coherent light sources for large-scale photonic integrated circuits [1]–[6]. These microdisk structures support whispering-gallery resonances that enable ultracompact and low-threshold laser operation. Electrically injected microdisk lasers have been demonstrated on InP substrates with threshold currents as low as 40 μA [6]. However, a cost-effective route to photonic integration should be based on a silicon platform, thereby exploiting the existing silicon processing infrastructure.

Recently, we achieved electrically injected continuous-wave lasing at room temperature in heterogeneous microdisk lasers coupled to a nanophotonic silicon-on-insulator (SOI) waveguide, with an emission wavelength of 1.6 μm [7]. The microlasers were fabricated in a thin InP-based film, directly bonded to the SOI wafer. A tunnel junction (TJ) was used for efficient carrier injection with low optical loss. Apart from the bonding, all the fabrication steps can be done on wafer scale, with conventional tools used for fabricating microelectronic integrated circuits. For fabrication details, we refer to [7]. A schematic drawing of the laser structure and a microscope image are shown in Fig. 1. A microdisk is etched in the InP-based layer, leaving a thin lateral bottom layer. The fundamental optical resonances in such a structure are whispering-gallery modes (WGMs), which are confined to the edges of the microdisk. Therefore, a top metal contact can be placed in the center of the microdisk, without adding extra optical losses. The bottom contact is positioned on a thin lateral contact layer: this layer

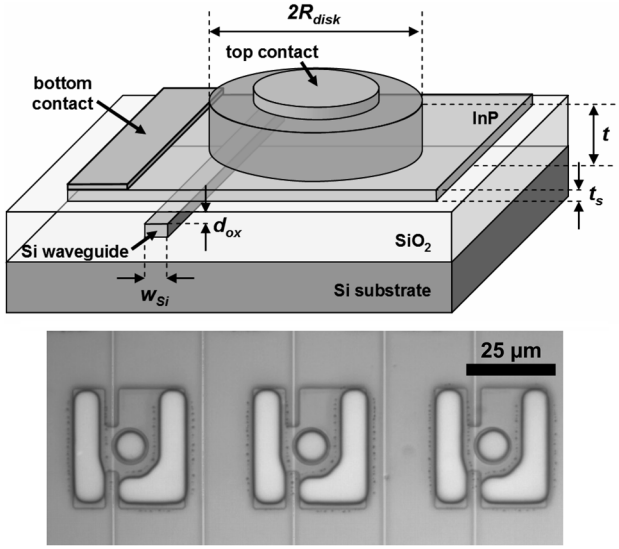

Fig. 1. Top: schematic drawing of the heterogeneous microdisk laser structure, showing the metal contact position and the output SOI wire waveguide. Bottom: optical microscope image of three fabricated microdisk lasers, just before the deposition of the metal contacts, showing the microdisk cavity, the InP bottom contact layer, the SOI wire, and the contact vias etched into the BCB planarization layer.

Manuscript received May 25, 2007; revised October 28, 2007. This work was supported in part by the EU-funded FP6-project PICMOS and by the FP6 network-of-excellence ePIXnet. The work of J. Van Campenhout was supported by the Research Foundation—Flanders (FWO-Vlaanderen) through a doctoral fellowship.

J. Van Campenhout, D. Van Thourhout, and R. Baets are with the Photonics Research Group, Department of Information Technology (INTEC), Ghent University-IMEC, 9000 Ghent, Belgium (e-mail: Joris.VanCampenhout@intec.UGent.be).

P. Rojo Romeo, P. Regreny, and C. Seassal are with the Institut des Nanotechnologies de Lyon, Université de Lyon, CNRS, Ecole Centrale de Lyon, 69134 Ecully, France.

L. Di Cioccio and J. M. Fedeli are with the CEA-DRT/LETI, 38054 Grenoble, France.

Digital Object Identifier 10.1109/JLT.2007.912107

will cause no substantial additional optical losses, provided it is sufficiently thin. The laser resonance is evanescently coupled to the underlying SOI waveguide, which is vertically aligned with the edge of microdisk. An important design aspect is the composition of the bonded InP-based film. It should enable efficient current injection, while preserving the optical resonance quality.

An efficient, compact and silicon-integrated electrically pumped laser is expected to find its use in on-chip optical interconnect [8]. To offer an advantage over electrical interconnect, the total power consumption of the optical link should be very low [9], requiring very low laser threshold current and low operating voltage [10]. Therefore, the goal of this work is to estimate the ultimate (static) laser performance that can be expected with this heterogeneous microdisk approach. In Section II, we optimize the InP-based epitaxial composition to obtain the lowest transparency gain, for a structure compatible with efficient electrical injection. In Section III, we investigate the bending loss to estimate the minimal microdisk laser size. In Section V, the optical coupling between the InP disk and the Si waveguide is analyzed, yielding a good estimate for required bonding layer thickness. The electrical injection performance is investigated in Section VI, where we pay attention to the lateral injection profile and the device voltage. Then, the optical and electrical data are combined in a straightforward laser model. This model is used in Section VII to optimize the main design parameters to maximize wall-plug efficiency. The model is then fitted to measured laser performance to test its viability (Section VIII). Finally, a conclusion is drawn in Section IX.

II. Thin-Film Epitaxial Layer Structure Design

The composition of the bonded epitaxial layers is of crucial importance for device performance: it should enable efficient carrier injection at low operating voltage while simultaneously provide light confinement with low internal absorption loss. The epitaxial layer should also be as thin as possible, since optical coupling to the underlying SOI waveguide is expected to be less efficient for thicker InP films. Thicker devices are also more difficult to etch with low surface roughness and to planarize, thus making integration more difficult. For the remainder of the paper, we shall impose an—arbitrary—upper film thickness of 1 μm. The major challenge in the epitaxial design lies in the requirement for low-voltage operation and high injection efficiency *together* with low internal optical loss. A major bottleneck for the electrical current could occur at the p-type contact. It is known that it is much more difficult to achieve low-resistance metal contacts to p-type InP as compared to n-type InP [11]. In traditional InP-substrate-based lasers, this is solved by using heavily p-type doped, low bandgap contact layers such as p++ InGaAs. These layers have large optical absorption, due to band-to-band absorption and/or free-carrier absorption (FCA), as highly p-type doped layers have large intervalence band absorption (IVBA). In classic substrate lasers, relatively thick ($> 1\,\mu$m) cladding layers provide optical isolation between the waveguide core and these very absorptive contact layers. It is clear that this approach cannot be used for thin-film microdisk lasers, since the internal losses would be excessive given the upper limit on the device thickness. Therefore, we should avoid large quantities of InGaAs and/or heavily p-type doped layers in the epitaxial structure, while preserving good electrical behavior. In the pedestal microdisk lasers presented in [1]–[4], current is injected in the disk through a central post that contains the p-type contact and doesn't overlap with the optical mode. However, due to the lack of current spreading layers, this injection scheme relies on carrier diffusion from the central region to the disk edge, resulting in limited (lateral) injection efficiency.

In our approach, a tunnel-junction is incorporated to efficiently contact the p-type diode layer, with low optical loss. As has been shown in the case of long-wavelength vertical-cavity surface-emitting lasers (VCSELs), TJs with a bandgap wavelength above the emission wavelength exhibit relatively low electrical resistance with only a minor optical loss penalty, provided that the TJ is well-positioned at a minimum of the optical field intensity and has adequate doping levels [12], [13]. Here, we investigate the performance of a TJ-based approach for the specific case of a thin-film microdisk laser and compare it with an approach based on a very thin InGaAs-contact layer [14]. The tunnel junction is assumed to consist of two 20-nm-thick, heavily doped (2×10^{19} cm^{-3}) InGaAsP layers with 1.2-μm bandgap wavelength (Q1.2). The active layer consists of three compressively strained $(+1.7\%)$ InAsP quantum wells, embedded in 20-nm-thick Q1.2 barriers, and surrounded with Q1.2 optical confinement layers (OCLs) with to-be-optimized thicknesses. Three designs are considered, as shown in Fig. 2. Design A has the active layer in the center of the epitaxial structure, with the TJ below the active layer and symmetric OCLs, with identical thickness t_1, that is to be optimized for given total thickness t. Design B has the TJ in the upper part of the structure, but with potentially asymmetric OCLs (thickness t_1 and t_2) around the active layer, which does not have to be in the center of the epitaxial structure. This design allows for reducing TJ-related optical absorption loss by reducing optical confinement in the TJ while preserving optical overlap with the quantum wells and the underlying SOI-waveguide. For a given total thickness t, t_1, t_2 and t_c should be optimized. Finally, design C is identical to design B except for the TJ and the top n-type contact layer which are replaced by a thin 15-nm p++ InGaAs contact layer and 100-nm p++ Q1.2 layer (3×10^{19} cm^{-3}). Each of the designs include an additional n-doped region (5×10^{18} cm^{-3}) with thickness $d_n = t/3$, and an additional p-doped region (5×10^{17} cm^{-3}) with thickness $d_p = t/7$, forming the pn-junction. Designs A and B have an additional n-type contact layer with thickness $t_n = 100$ nm. For each of the designs, the FCA is described by $\alpha = kP$ (in cm^{-1}), with P the doping level (in cm^{-3}) and k the loss coefficient. For n-type InP and InGaAsP we have used $k_n = 10^{-18}$ cm^2, while for p-type InP $k_p^{\mathrm{InP}} = 25 \times 10^{-18}$ cm^2 and for p-type InGaAsP $k_p^Q = 40 \times 10^{-18}$ cm^2 [15]. The OCLs are assumed to be filled with carriers with density $N_{\mathrm{OCL}} = t_{\mathrm{QW}}\tau_s/(t_{\mathrm{OCL}}\tau_e)N_{\mathrm{QW}}$, with t_{QW} the total thickness of the quantum wells, t_{OCL} the total OCL thickness, N_{QW} the carrier density in the quantum wells, τ_e the quantum well carrier escape time (25 ps), and τ_s the carrier diffusion time in the OCLs, given by $\tau_s = t_{\mathrm{OCL}}^{*2} q/4k_B T\mu_h$, with t_{OCL}^* the maximum of t_1 and t_2, q the elementary charge, k_B the Boltzmann constant, T the temperature (293 K) and μ_h

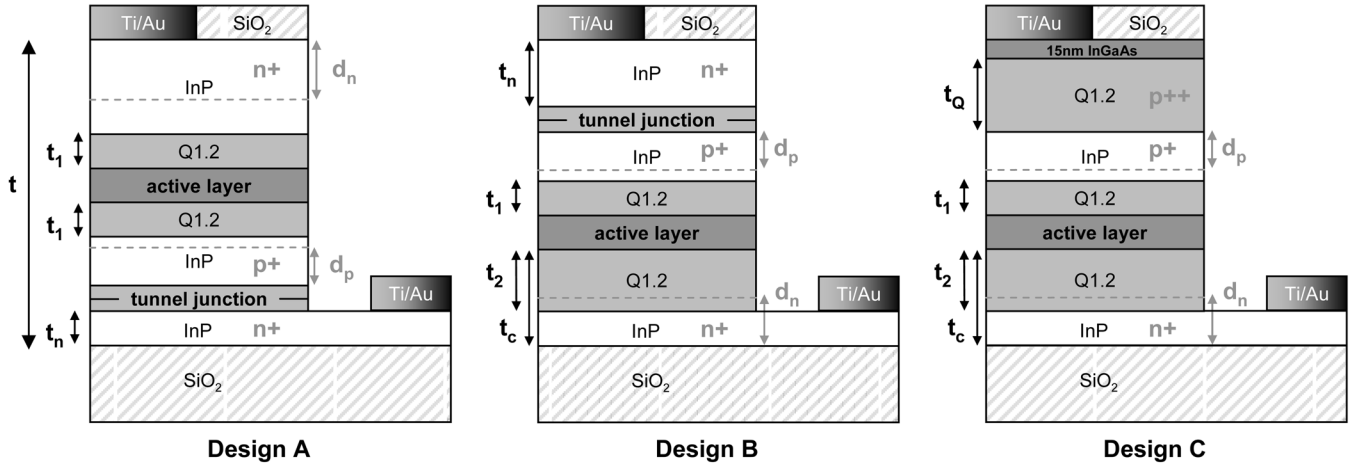

Fig. 2. Three epitaxial layer structure designs are under study: design A and B include a tunnel junction, whereas design C incorporates a thin ternary contact layer.

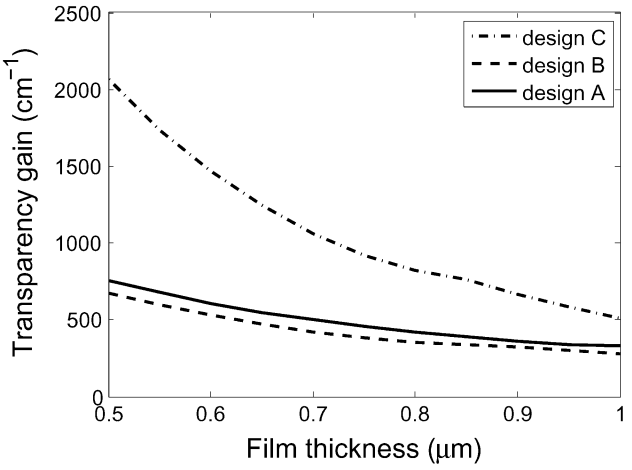

Fig. 3. Optimized transparency gain $G_{\rm tr}$ versus III-V film thickness t.

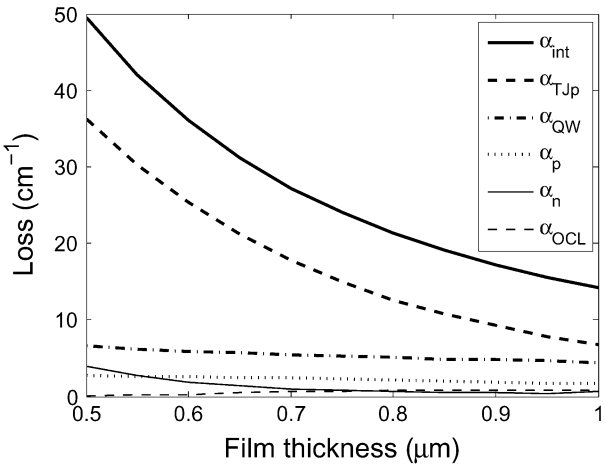

Fig. 4. Breakdown of the internal loss contributions for design A versus III-V film thickness t. $\alpha_{\rm int}$ is the total internal loss, $\alpha_{\rm TJp}$ is the loss in the p-side of the tunnel junction, $\alpha_{\rm QW}$ is the quantum-well contribution, $\alpha_{p/n}$ the loss in the diode p/n-doped layer and $\alpha_{\rm OCL}$ is the loss in the optical confinement layers.

the hole mobility in the OCL (70^2/Vs) [16]. While a rigorous analysis should contain a self-consistent determination of $N_{\rm QW}$, we have chosen a fixed value of 2.5×10^{18} cm^{-3}, which is a typical value at threshold.

For the three designs, we have optimized the relevant thicknesses to minimize the quantum-well material gain level that compensates for internal optical loss, calculated as $G_{\rm tr}=\alpha_{\rm int}/\Gamma_{\rm QW}$, with $\Gamma_{\rm QW}$ the optical confinement factor of the quantum wells, and $\alpha_{\rm int}$ the total internal loss. This was done for total film thicknesses in the range 0.5–1 μm, using a one-dimensional eigenmode-expansion technique [17]. The optimized $G_{\rm tr}$-values are shown in Fig. 3. For 500-nm-thick films, the TJ-based approaches A and B strongly outperform design C, with respective $G_{\rm tr}$-values of 755 cm^{-1}, 674 cm^{-1} versus 2061 cm^{-1}. For 1-μm-thick films, optimized $G_{\rm tr}$-values are, respectively, 330 cm^{-1}, 278 cm^{-1} versus 513 cm^{-1}. A breakdown of the loss contributions to the total internal loss for design A is shown in Fig. 4. For all thicknesses, the major contribution is due to IVBA in the p-side of the heavily doped TJ, followed by IVBA-losses in the quantum wells, in the p-region and n-region of the diode and in the OCLs. For the remainder of the paper, we will perform further device optimization for a *thin* (0.5 μm) and a *thick* (1 μm) benchmark structure, both based on design A. While design B has slightly lower $G_{\rm tr}$-values, design A is used in fabricated devices. To avoid dopant diffusion into the active layer, the heavily p-type doped TJ-layer should be grown as one of the last layers. Since the epitaxial layer is bonded after growth, the TJ will be located in between the active layer and the bonding interface.

In Section VII, the TJ p-doping is considered as an optimization parameter, so the internal loss is split into a TJ-specific part, and a fixed contribution $\alpha_{\rm int}^0$, containing the other losses. The total internal loss then reads

$$\alpha_{\rm int}=\alpha_{\rm int}^0+\Gamma_{TJp}k_p^Q N_a \tag{1}$$

with N_a the TJ p-type doping level, and $\Gamma_{\rm TJp}$ the confinement factor of the TJ p-side. An overview of the relevant parameters is given for both structures in Table I.

TABLE I
PARAMETERS FOR THE TWO BENCHMARK STRUCTURES

Parameter	Thin	Thick	Unit
t	0.5	1.0	μm
t_1	20	65	nm
α_{int}^0	13.3	7.5	cm^{-1}
Γ_{QW}	6.56	4.32	%
Γ_{TJp}	4.52	0.85	%

III. BENDING LOSS

Bending loss is typically very low for microdisk structures with a diameter of a few micrometer, given the high refractive index contrast between the disk and the surrounding medium (air). Ultracompact, pedestal-supported microdisk lasers with diameters as small as 2 μm have been demonstrated [2]. However, our design includes a thin lateral bottom contact layer with thickness t_s, which might introduce additional bending loss, especially for thick contact layers and small disk diameters. Also, the surrounding medium is Benzocyclobutene (BCB) rather than air, which favors higher bending loss as a result of the lower refractive index contrast. An assessment of the bending loss, defined with respect to the disk circumference, was performed using two different simulations tools. The first method is based on the commercial complex mode solver *FimmWave*. With this method, the bending loss can be calculated directly from the imaginary part of the effective index of the guided mode. The second tool uses two-dimensional finite-difference time-domain (FDTD) calculations, in cylindrical coordinates [18]. Here, we calculated the bending loss as

$$\alpha_b = \frac{2\pi n_g}{Q\lambda_0} \tag{2}$$

with Q the quality factor of the resonance, n_g the group index of the mode and λ_0 the vacuum wavelength. For the eigenmode-expansion calculations, λ_0 was set to 1.55 μm, while for the FDTD calculations, the resonant mode with wavelength closest to 1.55 μm was considered. A simplified disk structure was assumed, with a refractive index of 3.2 for the disk and contact layer, 1.44 for the SiO_2 and 1.54 for the BCB. The bending loss was calculated for the thin structure for three values of t_s: 0, 50, and 100 nm. Only the WGMs with the dominant **E**-field in the plane of the disk were considered (TE-modes). The results can be found in Fig. 5. The group index was set to 3.15, based on calculations for 7.5-μm-diameter disks. Good agreement was obtained between the two methods, with small deviations being caused by discretization errors, since the bending loss is very sensitive to disk radius and contact layer thickness. For the FDTD-simulations, a resolution of 20 nm was used, which is close to the dimension of the contact layer. For thick microdisks, bending loss behaves similarly, but is somewhat smaller. From these results, it is clear that the disk radius should be larger than 2.2 μm, assuming that t_s should be at least 50 nm for proper electrical operation, and tolerating a maximum bending loss of 1 cm^{-1}.

The radial mode intensity profiles $H_z^2(r)$ of the fundamental TE-polarized whispering-gallery modes, calculated with the eigenmode-expansion method at half microdisk thickness, are plotted in Fig. 5. It can be seen that the mode occupies a shell at the disk edge, with a width $W(R)$ in the range $0.2R - 0.5R$. It can be mathematically proven that the radial WGM profile matches with first-order Bessel function inside the disk, and a Hankel function outside the disk, with the boundary condition at the disk edge determining the exact mode shape [19]. For relatively large microdisks ($R > 2$ μm), the mode tail outside the disk is weak and the mode can be approximated with a Bessel function inside the disk and no field outside the disk. Such an approximation is used in Section VII and is illustrated by the dashed lines in Fig. 6.

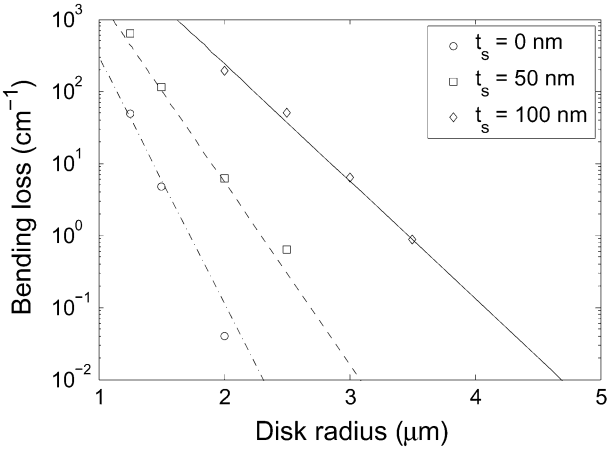

Fig. 5. Bending loss α_b for thin microdisks versus disk radius for different bottom contact layer thicknesses t_s. Lines represent eigenmode-expansion calculations, whereas the markers show FDTD results.

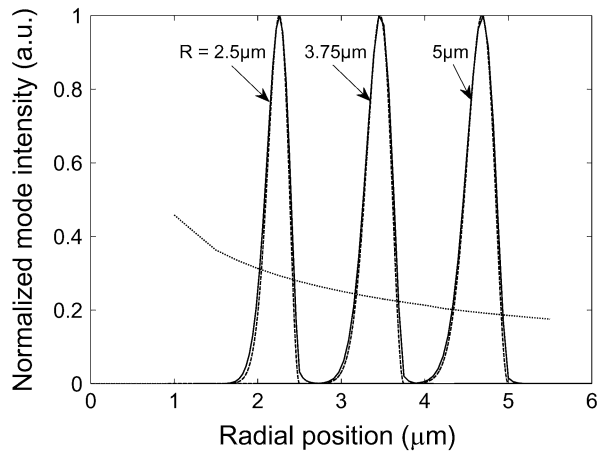

Fig. 6. Normalized $H_z^2(r)$-profiles for the fundamental TE-polarized whispering-gallery modes, as calculated by FimmWave for 5-μm, 7.5-μm and 10-μm microdisks (solid lines). A good approximation for $H_z(r)$ consists of a Bessel function inside the disk and a vanishing field outside the disk (dashed line). The dotted line represents the WGM width, as a fraction of disk radius.

IV. SCATTERING LOSS

For an assessment of the scattering loss that can be expected in our microdisk structures, we rely on the closed-form expression obtained by the volume-current method in [20]

$$\alpha_s = \frac{16\pi^3}{3R}\left(1 - \frac{n_0^2}{n_e^2}\right)^2 \left(\frac{n_e\sigma}{\lambda}\right)^2 \frac{n_e L_c}{\lambda}\Gamma_z \frac{t}{\lambda} \tag{3}$$

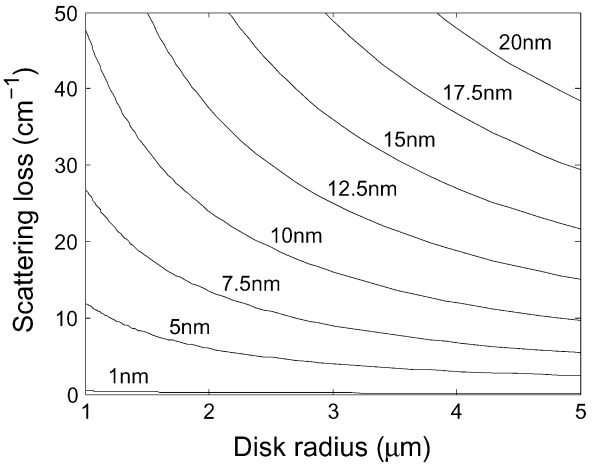

Fig. 7. Calculated scattering loss α_s for thick microdisks for different rms-values of the roughness σ, assuming a roughness correlation length $L_c = 100$ nm.

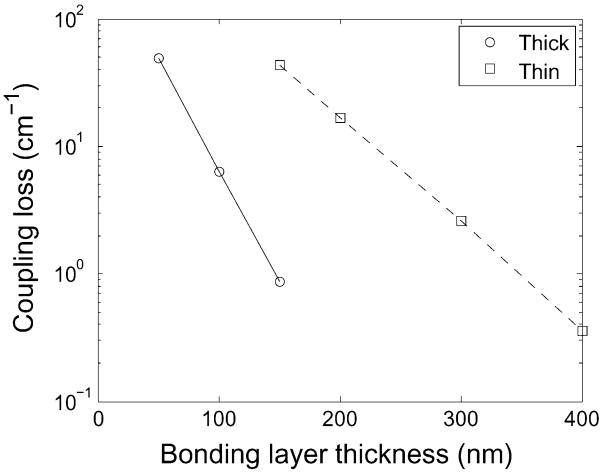

Fig. 8. Distributed coupling loss α_c for thin and thick microdisks with 7.5-μm diameter and a 500-nm-wide SOI wire waveguide (without offset) versus bonding layer thickness $d_{\rm ox}$.

where n_e is the effective index of the disk region, n_0 the index of the surrounding medium, σ the rms-value and L_c the correlation length of the edge roughness, and Γ_z the vertical disk confinement factor. In Fig. 7, α_s is plotted as a function of σ and R, for a 1-μm-thick film and assuming a roughness correlation length $L_c = 100$ nm. It can be seen that to suppress scattering loss, the roughness rms-value should be as low as 1 nm.

V. Coupling to the SOI Waveguide

In the previous sections, the optical losses were considered as parasitic and were to be minimized. Obviously, the coupling loss into the SOI waveguide is to be considered as a useful loss factor, and should be optimized for proper device operation. Here, we quantify this coupling loss as a function of the bonding layer thickness $d_{\rm ox}$, which is defined as the total SiO_2-thickness between the Si wire waveguide and the InP disk, the SOI wire waveguide width $w_{\rm Si}$ and the lateral offset between the InP disk and the Si waveguide. For zero lateral offset, the disk edge is assumed to be vertically aligned with the outer edge of the SOI wire. For a positive lateral offset, the waveguide shifts away from the microdisk center. The analysis is done for a fixed disk diameter of 7.5 μm. Three-dimensional FDTD calculations were performed, again for the simplified microdisk structure. The SOI wire waveguide is 500 nm or 600 nm wide and 220 nm thick. The Si refractive index was set to 3.48. First, the Q-factor was calculated for a microdisk without Si waveguide, being Q_0. Then, the calculations were repeated for structures with Si waveguide, yielding *loaded* quality factors Q_L. The quality factor Q_c due to coupling to the waveguide was then estimated as

$$Q_c = \left(\frac{1}{Q_L} - \frac{1}{Q_0}\right)^{-1}. \tag{4}$$

The distributed coupling loss α_c is then given by

$$\alpha_c = \frac{2\pi n_g}{Q_c \lambda_0}. \tag{5}$$

Only the fundamental resonances with wavelength in the range 1.55-1.6 μm were considered. The results for a 500-nm-wide SOI wire waveguide are shown in Fig. 8. For a given bonding layer thickness, coupling is much more efficient for the thin structures, as can be expected due to a better field overlap and improved phase matching of the InP disk mode with the Si waveguide mode. For the thick microdisk, a coupling loss of 20 cm^{-1} requires a 70-nm-thick bonding layer while a thin microdisk has the same coupling for a 190-nm-thick bonding layer. Moreover, the coupling is twice as sensitive to $d_{\rm ox}$ for thick structures as compared to the thin disks, what results in tighter fabrication tolerances on the bonding layer thickness. In Fig. 9, the coupling loss is shown as function of lateral waveguide-disk offset, for a thick microdisk and 500- and 600-nm-wide wires with a fixed bonding layer thickness of 100 nm. It can be seen that applying a lateral offset of 150- to a 500-nm-wide wire more than doubles the coupling efficiency, due to better phase matching. Increasing $w_{\rm Si}$ to 600 nm also improves the coupling efficiency, for the same reason. However, for this width, the SOI wire waveguide is no longer single mode. While FDTD images indicate dominant coupling to the fundamental wire mode, the wire should be tapered down to 500 nm to avoid mode conversion in the waveguide circuit. Lateral misalignment tolerances

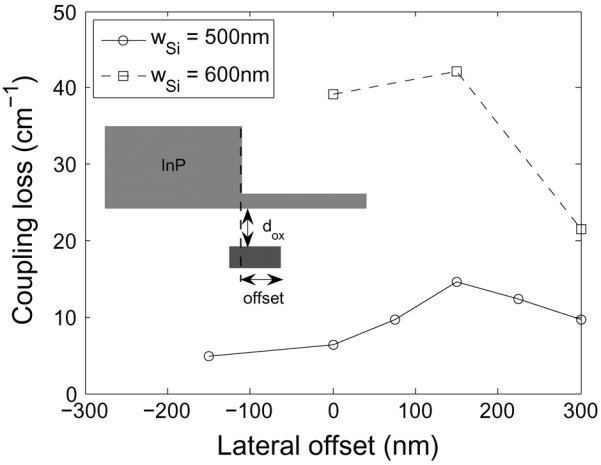

Fig. 9. Distributed coupling loss α_c for a thick 7.5-μm microdisk, a bonding layer thickness $d_{\rm ox} = 100$ nm and SOI wire waveguide widths $w_{\rm Si} = 500$ nm and 600 nm, versus lateral disk-wire offset.

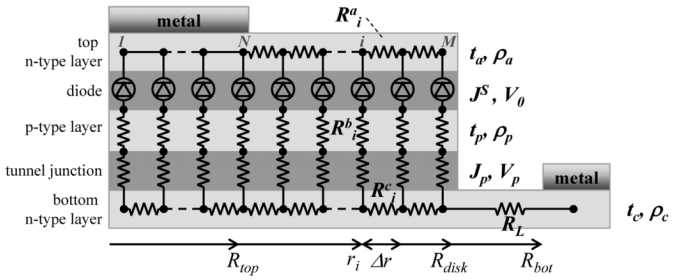

Fig. 10. Lumped electrical network, used for analyzing the current path in the microdisk laser.

are more relaxed as compared to the tolerance on the bonding layer thickness.

VI. Electrical Model

Efficient laser operation also requires efficient current injection and low operating voltage.

To analyze the current path in our TJ-based microdisk structure, we used an equivalent lumped circuit model as shown in Fig. 10. A two-dimensional network was used, exploiting the cylindrical symmetry of the disk. Another simplification was introduced by reducing the epitaxial layer structure to five functional layers, including an n-type contact and current spreading layer, a diode layer, a p-type layer, the tunnel-junction layer and a bottom n-type contact layer. Lateral current flow is expected to be mainly in the n-type layers, since they have the lowest effective resistivity. Lateral carrier diffusion was not taken into account. Each layer is characterized by its specific parameters. For the two n-type layers, the p-type layer and the diode layer, these are the thickness t_x of the layer and the resistivity ρ_x [11]. These parameters are then used to express the lumped resistors in the model

$$R_i^a = \rho_a \frac{\ln(r_i+\Delta r)-\ln(r_i)}{2\pi t_a}, r_i \geq R_{\text{top}} \tag{6}$$

$$= 0, \quad r_i < R_{\text{top}} \tag{7}$$

$$R_i^b = \frac{\rho_p t_p}{\pi[(r_i+\Delta r)^2 - r_i^2]} \tag{8}$$

$$R_i^c = \rho_c \frac{\ln(r_i+\Delta r)-\ln(r_i)}{2\pi t_c} \tag{9}$$

$$R_L = \rho_c \frac{\ln(R_{bot})-\ln(R)}{2\pi t_c} \tag{10}$$

with

$$\Delta r = R/M \tag{11}$$

$$r_i = \Delta r(i-1/2), \quad i = 1 \ldots M. \tag{12}$$

The diode layer is characterized as a carrier-controlled voltage source

$$V_i^{\text{diode}} = V_0 \ln\left(1+\frac{n}{n_e}\right) = V_0 \ln\left(1+\frac{I_i \tau_n}{q d_a A_i n_e}\right) \tag{13}$$

$$A_i = \pi\left[(r_i+\Delta r)^2 - r_i^2\right] \tag{14}$$

TABLE II
Parameter Values Used for the Electrical Analysis

	Thin	Thick	Unit			
ρ_a	17.5	25	$\mu\Omega$ m	R_c^{top}, R_c^{bot}	2.0	$10^{-5}\,\Omega\,\text{cm}^2$
ρ_c	10	15	$\mu\Omega$ m	τ_n	1	ns
t_p	100	220	nm	n_e	2.5	10^{11}cm^{-3}
ρ_p	3.0	3.0	mΩ m	n	2	
t_a	160	340	nm	N_d	1	10^{19}cm^{-3}
t_c	100	100	nm	N_a	2, 6, 20	10^{18}cm^{-3}
$R_{bot} = R$+3.75 μm				V_p, J_p	from [22]	

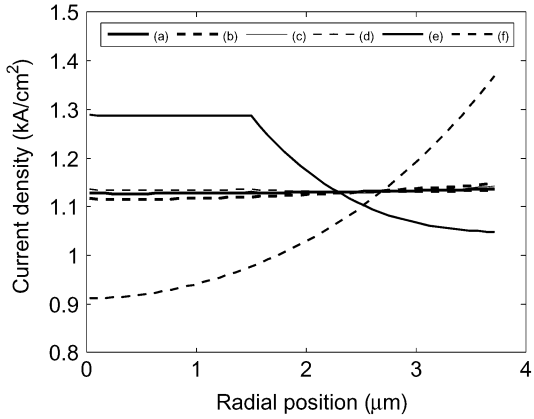

Fig. 11. Current density versus radial position calculated for a 7.5-μm disk, calculated with the network shown in Fig. 10, with the material parameters listed in Table II. Structures (a)–(d) include thick devices with $R_{\text{top}} = 0.4\,R$ or 0.8 R, and $N_a = 2 \times 10^{18}$ cm^{-3} or 2×10^{19} cm^{-3}, and show uniform current injection. Thin structures have comparable behavior. (e) has a 10-times-worse conducting top n-layer and a 10-times-better conducting bottom n-layer, while (f) has the opposite composition.

with n_e as the intrinsic carrier density in the active region, τ_n as the carrier lifetime, and $V_0 = nk_BT/q$ where n is the diode's ideality factor.

Finally, the tunnel-junction layer is assumed to obey the voltage-current characteristic [21]

$$J_i^{TJ} = J_p \left(\frac{V_i^{TJ}}{V_p}\right) \exp\left(1-\frac{V_i^{TJ}}{V_p}\right). \tag{15}$$

The parameters J_p and V_p depend on the bandgap and doping levels of the tunnel-junction layers. The explicit dependence was calculated in [22], for a similar tunnel junction, incorporated in a long-wavelength VCSEL. It was found that the TJ resistance decreases strongly with increasing p-doping level N_a in the TJ and with increasing bandgap wavelength of the TJ material, and to a lesser extent with increasing n-type doping level N_d. For our model, we rely upon the theoretical values for a 918-nm bandgap TJ presented in [22]. Since our design includes a Q1.2 TJ, we expect to overestimate device voltage.

The nonlinear system containing the electrical network equations with $M = 51$ nodes was numerically solved for a total input current of 0.5 mA, using the parameter values shown in Table II. The calculated current density as function of radial position is plotted in Fig. 11, for different TJ doping levels, top contact sizes (a-d). For all cases, the current density is uniform in good approximation, indicating efficient current spreading

in the n-type layers, even for $R_{\rm top} = 0.4R$ and low TJ resistance. Therefore, neglecting carrier diffusion should not have a big impact on the (subthreshold) injection profile. Two artificial, thick structures were also analyzed: structure (e) has a 10 times worse conducting top n-type layer and a 10–times-better conducting bottom n-type layer, while (f) has the opposite composition. The first case clearly has worse lateral injection performance, since for $r > R_{\rm top}$ the current preferably flows through the bottom n-type layer which has lower resistance. The latter has an increased injection density at the disk edge, which is advantageous for efficient laser operation, but it also has a 10 times bigger R_L resistance as compared to (a). Therefore, the benefit of such an approach to increase laser efficiency might be limited. For the remainder of the paper, we will assume uniform injection for both benchmark structures. Using this assumption, we now proceed with a more detailed assessment of the theoretical I-V characteristic. The device voltage contains contributions from the diode, the tunnel junction, the bottom contact layer, the metal-semiconductor contacts and current spreading

$$V(I) = V^{\rm diode}(I) + V^{TJ}(I) + (R_L + R_{\rm cont} + R_{CS})I \quad (16)$$

with

$$R_{\rm cont} = \frac{R_c^{\rm top}}{\pi R_{\rm top}^2} + \frac{R_c^{\rm bot}}{\pi\left((R_{\rm bot}+l_t)^2 - R_{\rm bot}^2\right)} \quad (17)$$

and R_L as defined in (10), $V^{TJ}(I)$ as in (15) and $V^{\rm diode}(I)$ as in (13), relative to the full microdisk area. $l_t = \sqrt{R_c^{\rm bot} t_c/\rho_c}$ is the carrier transfer length, which describes the effective length which carriers need to transfer from the metal into the semiconductor and vice versa. For the top contact, we assumed that the full contact area is used for carrier transfer. The metal contact resistivities $R_c^{\rm top}$ and $R_c^{\rm bot}$ were set to $5 \times 10^{-5}\Omega$ cm^2. The current spreading resistance $R_{\rm CS}$ is estimated to be $12\,\Omega$, based on the lumped network calculations. The calculated I-V curve for a thick 7.5-μm-diameter microdisk is shown in Fig. 12, for TJ p-doping levels N_a of 2×10^{18} cm^{-3}, 6×10^{18} cm^{-3} and 2×10^{19} cm^{-3}. Voltage contributions other than the diode voltage and TJ-voltage are lumped together in $V^{\rm other}$. The device voltage breakdown for $N_a = 2 \times 10^{18}$ cm^{-3} is also shown. For these low TJ p-doping levels, $V^{\rm TJ}$ clearly dominates $V^{\rm other}$. Increasing the TJ p-type doping level to $N_a = 2 \times 10^{19}$ cm^{-3} substantially decreases device resistance. However, as indicated in Section II, higher p-type doping increases internal loss. Therefore, the optimum doping level represents the best tradeoff between operating voltage and internal loss, and will be calculated in the next section.

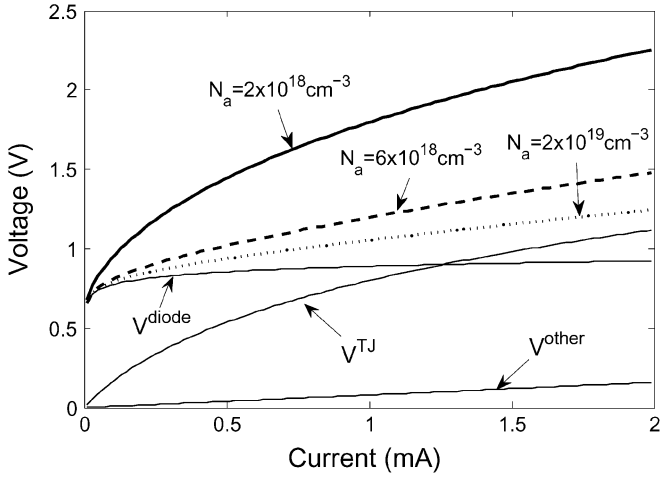

Fig. 12. Calculated IV curve for a thick 7.5-μm microdisk, assuming uniform injection, versus TJ p-doping level N_a. A breakdown of the device voltage is shown for $N_a = 2 \times 10^{18}$ cm^{-3}. For this doping level, the TJ-voltage dominates other nondiode related voltage contributions.

VII. Device Optimization

In this section, we combine the optical and electrical models obtained in the previous sections to optimize the global device performance. More specifically, we will optimize the disk radius R, coupling loss α_c and TJ p-type doping N_a to minimize the needed input power $P_{\rm in}$ for a given optical output power P_u. $P_{\rm in}$ can be written as

$$P_{\rm in} = VI \quad (18)$$

$$= V\left(I_{\rm th} + \frac{P_u q}{\eta_d h\nu}\right) \quad (19)$$

where $I_{\rm th}$ is the threshold current, η_d is the differential efficiency and ν is the laser frequency. We divide the microdisk in two regions: a central region for $r < R - W(R)$ and the edge region $R - W(R) < r < R$ which contains the laser mode (see Fig. 6). Therefore, the laser active volume can be written as $V_a = [\pi R^2 - \pi(R - W(R))^2]d_a$, with d_a the total quantum well thickness. Assuming uniform injection then results in a lateral injection efficiency $\eta_l = 2W(R)/R - W^2(R)/R^2$. Below threshold, we assume an additional, vertical injection efficiency $\eta_v = 0.9$, resulting in a subthreshold injection efficiency $\eta_i = \eta_v\eta_l$. For currents above laser threshold, we include a differential, vertical injection efficiency $\eta_v^d = 0.75$ [15], yielding a differential injection efficiency $\eta_i^d = \eta_v^d\eta_l$.

The total modal optical loss $\alpha_{\rm tot}$ can be written as

$$\alpha_{\rm tot} = \alpha_c + \alpha_b(R) + f(R)(\alpha_{\rm int}^0 + \Gamma_{\rm TJp} k_p^Q N_a) + \alpha_s(R) \quad (20)$$

with α_s the scattering loss at the disk edge and $f(R)$ a normalization factor that transforms the local internal loss to a modal loss defined with respect to the disk circumference, as are other loss contributions. $f(R)$ is calculated as

$$f(R) = \int_0^R H_z^2(r)\frac{r}{R}2\pi r dr \quad (21)$$

with $H_z^2(r)$ the radial laser mode profile. For these calculations, the whispering-gallery mode was approximated with a Bessel function of the first kind, as illustrated with the dashed lines in Fig. 6. The small mode tail outside the disk was neglected. For $R = 3.75$ μm, f is 0.8. For the calculation of the bending loss and bottom layer resistance R_L, t_s was fixed at 50 nm.

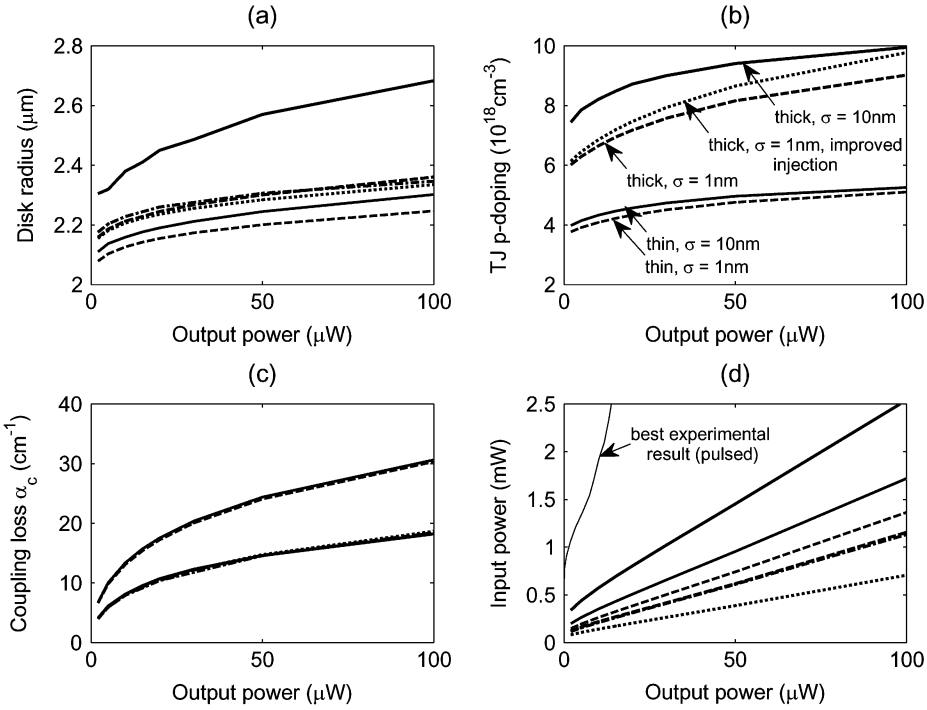

Fig. 13. Results of the optimization procedure both for the thin (gray) and thick epitaxial structure (black), for output powers in the range 1–100 μW. The optimized microdisk radius can be found in (a), the optimized tunnel-junction p-type doping in (b) and the optimized coupling loss in (c). The power consumption for devices with these optimized design parameters is shown in (d). Solid lines represent devices with roughness $\sigma = 10$ nm, $L_c = 100$ nm. The other cases have $\sigma = 1$ nm. The dotted line shows the results for an artificial structure with improved lateral injection efficiency ($\times 1.5$), whereas the dashed-dotted line represents optimized devices with the currently available estimated tunnel-junction optoelectronic performance, coinciding accidently with the dashed line. The best experimental result (pulsed regime) for a thick 7.5-μm-diameter microdisk laser is also shown, emphasizing the potential for device optimization.

The optical extraction efficiency η_e is given by

$$\eta_e = \frac{\alpha_c}{\alpha_{\text{tot}}} \tag{22}$$

and the bidirectional differential efficiency η_d is then

$$\eta_d = \eta_i^d \eta_e. \tag{23}$$

To obtain the unidirectional efficiency an additional factor $1/2$ should be added, since the ideal microdisk supports two degenerate, counterpropagating laser modes. For the optimization, light coupled into both directions is considered as useful output.

The threshold current can be written as

$$I_{\text{th}} = \left(An_{\text{th}} + Bn_{\text{th}}^2 + Cn_{\text{th}}^3\right) \frac{V_a q}{\eta_i} \tag{24}$$

where A is the Shockley-Read-Hall recombination coefficient $(10^8 s^{-1})$, B is the spontaneous recombination coefficient (2×10^{-10} cm^3 s^{-1}) and C is the Auger recombination coefficient (1.65×10^{-28} cm^6 s^{-1}). n_{th} is the carrier density at threshold, and is calculated as

$$n_{\text{th}} = n_0 \exp\left(\frac{\alpha_{\text{tot}}}{\Gamma_{\text{QW}} G_0 f(R)}\right) \tag{25}$$

where n_0 is the transparency carrier density (1.5×10^{18} cm^{-3}) and G_0 is the gain coefficient (1500 cm^{-1}). Clearly, the above expressions do not include gain suppression nor self-heating effects. While the latter causes early thermal roll-over in experimental devices, thereby limiting maximum output power, we believe that this effect can be suppressed by incorporating an adequate heat sinking structure, e.g., a thermal short connection between the top contact and the Si substrate.

The results of the optimization procedure are shown in Fig. 13, both for the thin (gray) and thick epitaxial structure (black), for output powers in the range 1–100 μW. Solid lines include devices with scattering loss for $\sigma = 10$ nm, the other cases have $\sigma = 1$ nm. The dotted line shows the results for an artificial structure with improved lateral injection efficiency ($\times 1.5$), which could be achieved by etching a hole or applying proton implantation in the center of the disk, thereby removing part of the leakage current. The dashed-dotted line represents ultimate performance with the estimated experimental tunnel-junction characteristics (see Section VIII). For all cases, the optimized disk radius is in the range 2.1–2.7 μm [Fig. 13(a)]. For smaller disks, the bending loss and/or scattering becomes the dominant optical loss mechanism. Optimized disk radii are slightly smaller for thin structures, since the internal loss is higher, allowing for a higher bending/scattering loss. The thick disks with $\sigma = 10$ nm have slightly bigger optimized disk radii, due to a higher α_s (which scales with t). The optimum TJ p-type doping N_a is for the thick structure in the range 6–10 $\times$ 10^{18} cm^{-3} (Fig. 13(b)), which results in theoretical operating voltages below 1.5 V. For the thin microdisks, optimized N_a-values are only 4–5 $\times$ 10^{18} cm^{-3}. Clearly, the larger Γ_{TJp} for the latter structures doesn't allow for very high N_a levels. The optimized coupling loss α_c ranges from 7 to 30 cm^{-1} for the thin structures and from 5 to 20 cm^{-1} for the thick microdisks [Fig. 13(c)]. A larger disk-waveguide coupling is needed for the thin microdisk lasers (about $\times 1.5$),

since the larger internal loss needs to be overcome to achieve decent differential efficiency. However, this can be obtained with relatively thicker bonding layers, as shown in Fig. 8, and with higher tolerance on the bonding layer thickness.

Finally, Fig. 13(d) shows the required electrical input power versus optical output power. For microdisks with substantial sidewall roughness, optimized thin microdisk lasers outperform thick structures, since the expression for scattering loss scales linearly with t. For thin (thick) devices, 50 μW output power would require an input power of 0.96 mW (1.45 mW), which is equivalent with 5.2% (3.4%) wall-plug efficiency (WPE). For $\sigma = 1$ nm, thick microdisks perform better: 50 μW output power would require 0.74 mW (6.8% WPE) and 0.61 mW (8.2% WPE) input power for the thin and thick microdisks, respectively. The better performance for the thick microdisk is due to the reduced optical overlap with the TJ p-side layer, but comes at the expense of a thinner optimum bonding layer thickness and the associated reduced tolerance. The hypothetical, thick device with improved lateral injection efficiency would only need 0.39 mW (12.8% WPE). Self-heating is expected to be less of a problem for this optimized device, since even with the thermal resistance of 10 K/mW for current experimental devices, temperature increase should remain under 10 °C for output powers up to 100 μW. Further WPE-improvement could be obtained by reducing the TJ layer thickness and by shrinking the microdisk diameter by using a isolation/planarization layer with lower refractive index than BCB.

VIII. Experimental Results and Discussion

Recently, we have fabricated SOI-integrated microdisk lasers, both in 0.55-μm-thick and 1-μm-thick bonded epitaxial structures. The microdisk diameters were 5 μm, 7.5 μm and 10 μm. Before metallization, the microdisk lasers were tested under optical pumping, and all devices exhibited lasing with sub-mW threshold powers and substantial coupling into the SOI waveguide. After BCB processing and metallization and a burn-in treatment, electrically pumped characterization was performed. Devices with variable top contact size (0.7–0.84R) were available. However, during fabrication, the top contact was misaligned by 400 nm. As a result, no lasing was observed for 5 μm-diameter microdisks. For the 7.5-μm and 10-μm devices, lasing in pulsed regime was observed for the microdisks with the smallest top contacts (0.7–0.76R). Lasing performance was poor for 10-μm devices, with threshold currents in the mA-range and low slope efficiency. However, for the 7.5-μm-diameter microdisk lasers, we found continuous-wave operation at room temperature (20 °C) [7]. The thick lasers were coupled to 565-nm-wide SOI wire waveguides with 125-nm-thick bonding layers. A typical set of measured LIV-data is shown in Fig. 14 (markers). CW operation was obtained for several devices with CW operating voltages below 2 V, typical threshold currents in the range 500–600 μA, and slope efficiencies just above threshold in the range 10–30 μW/mA, depending on the top contact size and lateral SOI waveguide offset. The maximum CW unidirectional output power was found to be 10 μW, being limited by an early thermal roll-over due to the high thermal resistance. In pulsed regime, the peak output power can be considerably higher (tens of μW).

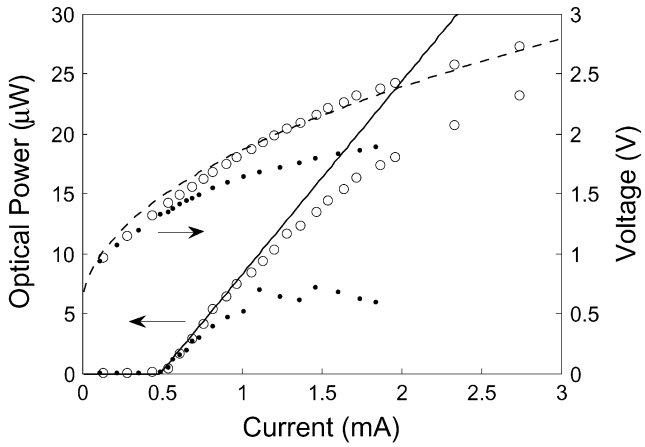

Fig. 14. Experimental data for a 7.5-μm-diameter microdisk laser (markers), and fit to the experiment (lines). The solid line represents unidirectional output power, the dashed line shows device voltage. Circles denote pulsed measurements, dots are in continuous wave.

To test our theoretical model, we now consider only the lasing performance in pulsed regime (100-ns pulses, 5-μs period), since for such measurements, self-heating effects should be suppressed. The presented LIV-data is for a microdisk with a 0.72 R-radius top contact and a lateral SOI wire offset of -100 nm. The theoretical model can be fitted to the date using the simulated value $\alpha_c = 3.1$ cm^{-1} for coupling loss, and assuming $\alpha_s = 9$ cm^{-1} and $N_a = 2 \times 10^{18}$ cm^{-3}. For these values, the theoretical model provides a very good fit for the voltage and also for the output power, except for the saturation at high pumping levels. The scattering loss of 9 cm^{-1} is in agreement with extracted scattering loss in passive InP-based ring resonators [23], and is equivalent with a roughness $\sigma \sim 8$ nm, $L_c = 100$ nm, according to (3). The fitted TJ doping N_a however is one order of magnitude lower than the designed value. We note that the extracted experimental TJ performance is very similar to the experimental data presented in [12], even though the TJ material composition is not identical. However, for our devices, a secondary ion mass spectrometry (SIMS) analysis on similar TJ-test-structures indicates that the maximum TJ p-doping is at least 8×10^{18} cm^{-3}. We speculate that a nonabrupt doping profile—due to dopant diffusion—results in an effective, fitted N_a-value of 2×10^{18} cm^{-3} to be used in the electrical TJ-model. However, such a suboptimal doping profile would still cause IVBA-loss scaled with the total amount of p-dopants. Therefore, we believe that the fitted scatter loss contains some TJ-related internal IVBA-loss. Considering these assumptions, we performed another optimization using an effective N_a-value of 2×10^{18} cm^{-3} for the electrical TJ performance and a real $N_a = 8 \times 10^{18}$ cm^{-3} for TJ IVBA loss, and improved lateral injection efficiency. The results are shown in Fig. 13 (dashed-dotted line), and are very similar to the optimized devices with theoretical TJ-performance but without improved injection. This performance could be considered as a near-term goal, since it could be achieved with the opto-electronic performance of the currently available TJ, provided

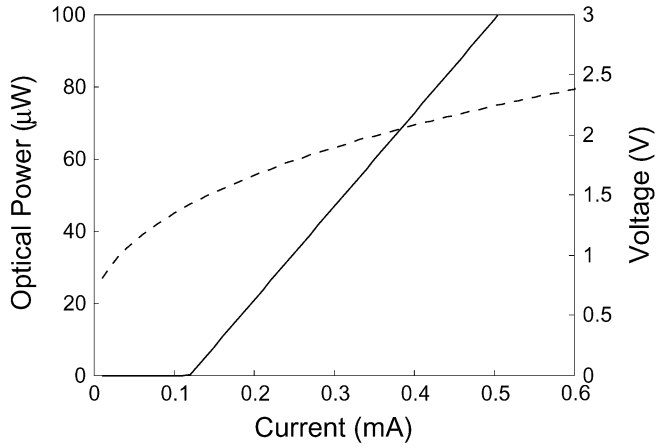

Fig. 15. Theoretical LIV-data for microdisk laser optimized for 50 μW output power with current estimated experimental TJ performance.

that we can optimize the coupling, reduce scattering loss and improve injection efficiency. The calculated LIV-curves for such a near-term device, optimized for 50 μW output power are shown in Fig. 15. It has a radius of 2.3 μm, a threshold current of 120 μA, a slope efficiency of 260 μW/mA and operates under 2 V for the targeted output power.

The power saturation at higher output power cannot be explained by our (simple) model. Clearly, the injection efficiency drops with increasing pumping level. Such behavior is typical for pedestal-supported microdisk lasers with central injection, which rely on carrier diffusion to get carriers from the microdisk center to the laser region. For such devices, the lateral injection efficiency decreases with the pumping level, due to an increase in nonradiative recombination in the center of the device as a result of the lack of carrier clamping in that region. Based on the calculations for the electrical lumped-network model which indicate uniform injection, we wouldn't expect this effect in our devices. However, our simple electrical model doesn't account for the noncylindro-symmetrical shape of the bottom contact, as shown in Fig. 1. Therefore, we speculate that the saturation effect is caused by current crowding in some parts of the microdisk, as a result of this asymmetry. A full three-dimensional electrical analysis should be performed to bring more insight into this saturation effect. Anyhow, we believe that the impact of this effect on device performance should be small for a fully optimized device with symmetrical bottom contacts and adequately aligned top contacts.

IX. Conclusion

A numerical study of InP-based microdisk lasers integrated on and coupled to a nanophotonic SOI waveguide circuit was performed. First, the composition of the epitaxial layer structure was optimized to minimize transparency gain values. It was found that a tunnel-junction based approach outperforms an approach based on a thin ternary contact layer, both for thin (0.5 μm) and thick (1.0 μm) structures. Bending loss was quantified with a complex mode solver and a FDTD tool, revealing a minimum microdisk diameter of 4.4 μm, assuming BCB planarization. The coupling between the InP microdisk and Si waveguide was studied as function of the bonding layer thickness, waveguide offset and waveguide width. For the thin microdisk, a 200-nm-thick bonding supports adequate optical coupling whereas a thick microdisk requires a 100-nm-thick bonding layer. The lateral injection efficiency was studied with an equivalent electrical network. Uniform current injection is expected for the used epitaxial composition, under the assumption of cylindrical symmetry. The theoretical *I–V* characteristic was calculated, yielding operating voltages below 2 V for moderate tunnel-junction doping levels. Based on these results, the dominant device parameters were identified: microdisk thickness, radius, coupling loss and tunnel-junction p-type doping. These parameters were then optimized to obtain maximum wall-plug efficiency, for output powers in the range 1–100 μW. A fully optimized microdisk laser was found to have a diameter of less than 5 μm with a theoretical wall-plug efficiency of more than 10%. Finally, the theoretical model was tested by fitting it to experimental lasing characteristics. A good fit was obtained using parameter values that are consistent with numerical simulation. We conclude that this device has great potential for cost-effective on-chip optical functionality, such as optical interconnect.

Acknowledgment

The authors would like to thank S. Verstuyft, J. Van Den Troost, and L. Van Landschoot for the part of the III-V processing of the devices, and J. Van Campenhout for fruitful discussion on the electrical modeling.

References

[1] A. F. J. Levi, R. E. Slusher, S. L. Mccall, T. Tanbun-Ek, D. L. Coblentz, and S. J. Pearton, "Room-temperature operation of microdisk lasers with submilliamp threshold current," *Electron. Lett.*, vol. 28, no. 11, pp. 1010–1012, 1992.

[2] T. Baba, M. Fujita, A. Sakai, M. Kihara, and R. Watanabe, "Lasing characteristics of GaInAsP-InP strained quantum-well microdisk injection lasers with diameter of 2–10 μm," *IEEE Photon. Technol. Lett.*, vol. 9, no. 7, pp. 878–880, 1997.

[3] M. Fujita, A. Sakai, and T. Baba, "Ultrasmall and ultralow threshold GaInAsP-InP microdisk injection lasers: Design, fabrication, lasing characteristics, and spontaneous emission factor," *IEEE J. Sel. Topics Quantum Electron.*, vol. 5, no. 3, pp. 673–681, 1999.

[4] R. Ushigome, M. Fujita, A. Sakai, T. Baba, and Y. K. Kubun, "GaInAsP microdisk injection laser with benzocyclobutene polymer cladding and its athermal effect," *Japan. J. Appl. Phys.*, vol. 41, no. 11A, pp. 6364–6369, 2002.

[5] S. J. Choi, K. Djordjev, S. J. Choi, and P. D. Dapkus, "Microdisk lasers vertically coupled to output waveguides," *IEEE Photon. Technol. Lett.*, vol. 15, no. 10, pp. 1330–1332, 2003.

[6] M. Fujita, R. Ushigome, and T. Baba, "Continuous wave lasing in GaInAsP microdisk injection laser with threshold current of 40 ua," *Electron. Lett.*, vol. 36, no. 9, pp. 790–791, 2000.

[7] J. Van Campenhout, P. Rojo-Romeo, D. Van Thourhout, C. Seassal, P. Regreny, L. Di Cioccio, J. M. Fedeli, C. Lagahe, and R. Baets, "Electrically pumped InP-based microdisk lasers integrated with a nanophotonic silicon-on-insulator waveguide circuit," *Opt. Express*, vol. 15, no. 11, pp. 6744–6749, 2007.

[8] D. A. B. Miller, "Rationale and challenges for optical interconnects to electronic chips," *Proc. IEEE*, vol. 88, no. 6, pp. 728–749, 2000.

[9] M. Haurylau, G. Q. Chen, H. Chen, J. D. Zhang, N. A. Nelson, D. H. Albonesi, E. G. Friedman, and P. M. Fauchet, "On-chip optical interconnect roadmap: Challenges and critical directions," *IEEE J. Sel. Topics Quantum Electron.*, vol. 12, no. 6, pp. 1699–1705, 2006.

[10] I. O'Connor, F. Tissafi-Drissi, F. Gaffiot, J. Dambre, M. De Wilde, J. Van Campenhout, D. Van Thourhout, J.-M. Van Campenhout, and D. Stroobandt, "Systematic simulation-based predicitve synthesis of integrated optical interconnect," *IEEE Trans. Very Large Scale Integr. (VLSI) Syst.*, 2007, to be published.

[11] T. P. Pearsall, *Properties, Processing and Applications of Indium Phosphide*, ser. Emis datareview. London, U.K.: IEE , 2000.
[12] J. Boucart, C. Starck, F. Gaborit, A. Plais, N. Bouche, E. Derouin, J. C. Remy, J. Bonnet-Gamard, L. Goldstein, C. Fortin, D. Carpentier, P. Salet, F. Brillouet, and J. Jacquet, "Metamorphic DBR and tunnel-junction injection: A CW RT monolithic long-wavelength VCSEL," *IEEE J. Sel. Topics Quantum Electron.*, vol. 5, no. 3, pp. 520–529, 1999.
[13] M. Ortsiefer, S. Baydar, K. Windhorn, G. Bohm, J. Rosskopf, R. Shau, E. Ronneberg, W. Hofmann, and M. C. Amann, "2.5-mw single-mode operation of 1.55-mu m buried tunnel junction VCSELs," *IEEE Photon. Technol. Lett.*, vol. 17, no. 8, pp. 1596–1598, 2005.
[14] M. Vanwolleghem, P. Gogol, P. Beauvillain, W. Van Parys, and R. Baets, "Design and optimization of a monolithically integratable InP-based optical waveguide isolator," *J. Opt. Soc. Amer. B-Opt. Phys.*, vol. 24, no. 1, pp. 94–105, 2007.
[15] J. Piprek, *Semiconductor Optoelectronic Devices. Introduction to Physics and Simulation*. San Diego, CA: Elsevier, 2003.
[16] M. Irikawa, T. Ishikawa, T. Fukushima, H. Shimizu, A. Kasukawa, and K. Iga, "Improved theory for carrier leakage and diffusion in multi-quantum-well semiconductor lasers," *Japan. J. Appl. Phys.*, vol. 39, no. 4A, pp. 1730–1737, 2000.
[17] P. Bienstman and R. Baets, "Optical modelling of photonic crystals and VCSELs using eigenmode expansion and perfectly matched layers," *Opt. Quantum Electron.*, vol. 33, no. 4–5, pp. 327–341, 2001.
[18] A. Farjadpour, D. Roundy, A. Rodriguez, M. Ibanescu, P. Bermel, J. D. Joannopoulos, S. G. Johnson, and G. W. Burr, "Improving accuracy by subpixel smoothing in the finite-difference time domain," *Opt. Lett.*, vol. 31, no. 20, pp. 2972–2974, 2006.
[19] A. Morand, K. Phan-Huy, Y. Desieres, and P. Benech, "Analytical study of the microdisk's resonant modes coupling with a waveguide based on the perturbation theory," *J. Lightw. Technol.*, vol. 22, no. 3, pp. 827–832, 2004.
[20] J. Heebner, T. C. Bond, and J. S. Kallman, "Generalized formulation for performance degradations due to bending and edge scattering loss in microdisk resonators," *Opt. Express*, vol. 15, no. 8, pp. 4452–4473, 2007.
[21] T. A. Demassa and D. P. Knott, "The prediction of tunnel diode voltage-current characteristics," *Solid-State Electron.*, vol. 13, no. 2, pp. 131–138, 1970.
[22] M. Mehta, D. Feezell, D. A. Buell, A. W. Jackson, L. A. Coldren, and J. E. Bowers, "Electrical design optimization of single-mode tunnel-junction-based long-wavelength VCSELs," *IEEE J. Quantum Electron.*, vol. 42, no. 7–8, pp. 675–682, 2006.
[23] I. Christiaens, "Vertically coupled microring resonators fabricated with wafer bonding," Ph.D. thesis, Ghent Univ., Ghent, Belgium, 2005.

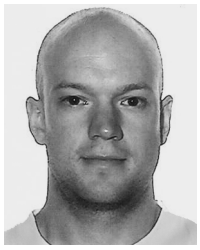

Joris Van Campenhout (S'01) received the degree in physics engineering form Ghent University, Ghent, Belgium, in 2002.

He is currently working toward the Ph.D. degree in electrical engineering with the Photonics Research Group of the same institution. His research interests include the design, fabrication, and characterization of silicon-based photonic integrated circuits. Over the past years, he has been working on the heterogeneous integration of InP-based microcavity lasers—based on photonic-crystal and microdisk structures—on a silicon platform.

Pedro Rojo Romeo was born in Madrid, Spain, in 1958. He received the InG. Dipl. degree in 1981 and the Ph.D. degree in electronic devices in 1984 from the Institut National des Sciences Appliquées (INSA), Lyon, France.

He is currently an Associate Professor in electronics with Ecole Centrale de Lyon, France. His primary research interests include electrical and optical devices fabrication technology, characterization of microelectronic and optoelectronic micro—nano devices. He is also involved in optical interconnection systems, nanotechnologies, and optical integrated circuits technologies.

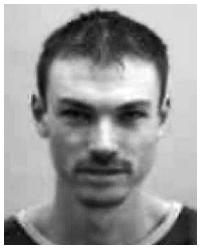

Dries Van Thourhout (M'98) received the degree in physical engineering and the Ph.D. degree from Ghent University, Ghent, Belgium, in 1995 and 2000, respectively.

From October 2000 to September 2002, he was with Lucent Technologies, Bell Laboratories, NJ, working on the design, processing, and characterization of InP/InGaAsP monolithically integrated devices. In October 2002, he joined the Department of Information Technology (INTEC), Ghent University, where he is currently a member of the Photonics Group. He is a lecturer or co-lecturer for four courses within the Ghent University Master in Photonics program (Microphotonics, Advanced Photonics Laboratory, Photonic Semiconductor Components, and Technology). He is also coordinating the cleanroom activities of the research group. His research focuses on the design, fabrication, and characterization of integrated photonic devices. Main topics involve silicon nanophotonic devices, heterogeneous integration of InP-on-Silicon, and integrated InP-based optical isolators. He is also working on the development of new fabrication processes for photonic devices, e.g., based on focused ion beam etching and die-to-wafer bonding. He holds three patents, has authored and coauthored more than 30 journal papers, and has presented invited papers at several major conferences.

Christian Seassal graduated from the Insitut National des Sciences Appliquees, (INSA), Lyon, France, in 1993, and received the Ph.D. degree in condensed matter in 1997 from Ecole Centrale, (ECL), Lyon.

He has been a CNRS research scientist since 1998, now in the Nanophotonics group, Lyon Nanotechnology Institute (INL, a joint research unit between CNRS, ECL, INSA, and the University of Lyon). His research activities concern active integrated micro-nanophotonic structures and MOEMS. His recent experiments deal with photonic crystal lasers and nonlinear devices, quantum dots nanophotonic devices, heterogeneous integration between active III-V photonic devices, and silicon photonic circuits. He is the author and coauthor of approximately 50 papers in international journals and 70 international conferences.

Philippe Regreny was born in France in 1967. He received the M.Sc. degree in materials science from Rennes University. He received the Ph.D. degree in electronics from Ecole Centrale de Lyon, France, in 1997.

He is now a research engineer with INL/CNRS, Ecole Centrale de Lyon. His current research interests concern epitaxial growth of III-V semiconductor compounds and their integration on silicon.

Léa Di Cioccio received the degree in physics engineering and the M.S. degree in metallurgy and material science in 1985 from the INSA Rennes and Paris VI University France, respectively. She received the Ph.D. degree in material and semiconductor physics from the INP Grenoble , France, in 1988.

She joined the CEA-LETI, Grenoble , in 1990 and is currently a specialist in semiconductor material heterostructures and 3-D integration using various processes such as epitaxy, wafer bonding, and Smart CutTM process. She has been engaged in characterization such as transmission electron microscopy. She is the author and coauthor of more than 100 publications and 15 patents.

Jean-Marc Fedeli received the electronics engineer diploma from INPG Grenoble, France, in 1978.

He has conducted research with the CEA-LETI, Grenoble, on various magnetic memories and magnetic components as project leader, group leader, and program manager. For two years, he was Advanced Program Director in the Memscap company for the development of RF-MEMS. He then returned to CEA-LETI in 2002 as Coordinator of Silicon Photonic Projects. Under a large partnership with universities and research laboratories, he works on various technological aspects on photonics on CMOS (Si rib and stripe waveguides, Si3N4, and a-Si waveguides), Si modulators, Ge photodetectors, SiOx material, and InP sources on Si. His main focus is on the integration of a photonic layer at the metallization level of an electronic circuit.

Roel Baets (M'88–SM'96–F'02) received the degree in electrical engineering from Ghent University, Ghent, Belgium, in 1980. He received the M.Sc. degree in electrical engineering from Stanford University, Stanford, CA, in 1981 and the Ph.D. degree from Ghent University in 1984.

Since 1981 he has been with the Department of Information Technology (INTEC), Ghent University. Since 1989, he has been a professor in the engineering faculty of Ghent University. From 1990 to 1994, he has also been a part-time professor with the Technical University of Delft, The Netherlands. Since 2004, he is also a part-time professor with the Technical University of Eindhoven, The Netherlands. He has mainly worked in the field of photonic components. With about 200 journal publications and 400 conference papers, as well as about 10 patents, he has made contributions to research on III-V semiconductor laser diodes, passive guided wave and grating devices, and to the design and fabrication of photonic ICs. He leads the Photonics Research Group of Ghent University-INTEC (associated lab of IMEC), which focuses on new concepts for photonic components and circuits for optical communication, optical interconnect, and optical sensing. He has been involved in various European research projects and has been coordinator of some of them. Currently, he coordinates the European Network of Excellence ePIXnet.

Dr. Baets is a member of the Optical Society of America, IEEE-LEOS, SPIE, and the Flemish Engineers Association. He has been member of the program committees of a.o. OFC, ECOC, IEEE Semiconductor Laser Conference, ESSDERC, CLEO-Europe, LEOS Annual Meeting, Photonics Europe, and ECIO. He has been chairman of the IEEE-LEOS-Benelux chapter from 1999 to 2001. From 2003 to 2005, he was an elected member of the Board of Governors of IEEE-LEOS.